Atmospheric Research 281 (2023) 106492

Contents lists available at ScienceDirect

Atmospheric Research

journal homepage: www.elsevier.com/locate/atmosres

Investigation on cloud vertical structures based on Ka-band cloud radar observations at Wuhan in Central China

Junjie Fang [a,b], Kaiming Huang [a,b,c,*], Minkang Du [a,b], Zirui Zhang [a,b], Rang Cao [a,b], Fan Yi [a,b,c]

[a] School of Electronic Information, Wuhan University, Wuhan, China
[b] Key Laboratory of Geospace Environment and Geodesy, Ministry of Education, Wuhan, China
[c] State Observatory for Atmospheric Remote Sensing, Wuhan, China

ARTICLE INFO

Keywords:
Ka-band cloud radar
Cloud base and top heights
Cloud and precipitation occurrence frequencies
Wuhan in Central China

ABSTRACT

Based on vertically pointing observations of Ka-band frequency-modulated continuous millimeter wave cloud radar (MMCR) in 2020, we investigate cloud vertical structures at Wuhan in central China. Case comparison indicates that the cloud top locations in the MMCR observation are largely consistent with those in satellite data. The precipitation has the occurrence frequency of 9.5% over the year, with the maximum value of 16.3% in July and the submaximal value of 14.7% in January, showing the significant influences of monsoons on precipitation at Wuhan. As the humid, cloudy and rainy climate, the probability of precipitation and non-precipitation clouds increases gradually from 53.9% in January to a large value of 71.5% in July. The non-precipitation clouds have the probability of 44.5% in the year, with two prominent peaks at the reflectivities of −35 to −30 dBZ around 12 km in summer and − 37– −32 dBZ around 10 km in spring. The cloud top can reach the heights of 14.49, 16.62, 13.38 and 11.73 km from spring to winter, respectively. The monthly mean cloud layer thickness is the largest (2.18 km) in May and September, and the smallest (1.36 km) in November. The seasonally averaged base and top heights and thickness of clouds have small diurnal variations. The high cloud is predominant in the warm months from May to September, and in the other cool months, the middle cloud has the most fraction. The quantitative investigation of clouds is helpful in improving the cloud parameterization in climate models.

1. Introduction

Clouds play an essential role in the Earth's atmospheric system because they affect the energy budget by reflecting radiation from the Sun and the Earth's surface and are a significant phase in the hydrological cycle accompanied by latent heat release (Quante, 2004; Stephens, 2005; Huang, 2013). The features of cloud vertical structures, such as cloud base height (CBH), cloud top height (CTH), cloud layer thickness (CLT), and cloud occurrence frequency (COF), are important in quantitatively describing the radiation impact of clouds on the climate system (Wang and Rossow, 1998; Zhang et al., 2019). CBH and CTH determine the incident flux at the cloud boundaries, and COF and CLT are an uncertainty in the calculation of longwave radiation reflected by clouds and corresponding heating rate in the presence of clouds (Ellingson, 1982; Han and Ellingson, 2000; Hawkinson et al., 2005; Zhou et al., 2021). During the periods of precipitation, precipitation intensities are associated with cloud height and thickness and their evolution. Therefore, the investigation of cloud vertical structures can help us to fully understand the radiative influence of clouds and the relation between precipitation and clouds (Clothiaux et al., 1999; Yan et al., 2016).

A large number of observations from ground-based and satellite-borne remote sensing and in situ detection have been used to evaluate the characteristics of clouds over the last few decades (Newell et al., 1972; Winker and Vaughan, 1993; Lazarus et al., 2000; Chang and Li, 2005; Minnis et al., 2008; Xi et al., 2010; Alexander and Protat, 2018; Cairo et al., 2021; Guo et al., 2021). Chang and Li (2005) presented the global statistics of COF, cloud top pressure and temperature, visible optical depth, and infrared emissivity from the data obtained by multiple channel Moderate-resolution Imaging Spectroradiometer (MODIS) deployed on Terra. Nazaryan et al. (2008) analyzed the seasonal variation of cirrus clouds based on Cloud-Aerosol Lidar and Infrared Pathfinder Satellite Observations (CALIPSO) data. Using the measurements from space-borne CloudSat radar, cloud classification and vertical structure properties of cirriform, anvil, and deep convective clouds were studied (Sassen and Wang, 2008; Stephens et al., 2008; Young et al.,

* Corresponding author at: School of Electronic Information, Wuhan University, Wuhan, China.
E-mail address: hkm@whu.edu.cn (K. Huang).

https://doi.org/10.1016/j.atmosres.2022.106492
Received 21 July 2022; Received in revised form 25 October 2022; Accepted 25 October 2022
Available online 28 October 2022

2013). Although CloudSats provide the global distribution of cloud cover, they cannot measure the diurnal variation of cloud due to their sparse temporal resolution. From surface-based Raman depolarization lidar observation, Alexander and Protat (2018) determined cloud boundaries, cloud phase and ice virga, which showed that surface-based lidar has a low sensitivity for detecting precipitating ice. Martucci et al. (2010) discussed multilayer CBH retrievals from the vertical profiles of backscattered laser signal from two collocated ceilometers by combining cloud base product outputted by the two instruments. Radiosondes with high accuracy and vertical resolution were widely used to obtain meteorological parameters through in situ sounding with ascending balloon, thus radiosonde observations are applied to investigating cloud vertical structures (Zhang et al., 2010). Poore et al. (1995) derived the location of cloud boundaries by testing for dewpoint temperature depressions below some threshold values from rawinsonde measurements. Winker and Vaughan (1993) investigated vertical distribution of clouds, especially cirrus, observed by lidar. Nevertheless, radiosondes are routinely released only twice a day, and it is generally difficult for ceilometer and lidar to observe cloud top because of severe attenuation by cloud and precipitation particles (Clothiaux et al., 2000; Chang and Li, 2005; Xi et al., 2010). Hence, cloud radars were developed to continuously observe cloud vertical structures.

Cloud radars usually operate at millimeter bands with high temporal and spatial resolution. Compared with centimeter band weather radar, millimeter wave cloud radar (MMCR) is more suitable for observing non-precipitation clouds and weak precipitation clouds because of its high sensitivity to cloud particles (Moran et al., 1998; White et al., 1996). Meanwhile, relative to optical instruments, MMCR can obtain more vertical cloud information, in particular, for thick clouds, dense clouds, and multilayer clouds, due to its fine penetrability of clouds (Krofli and Kelly, 1996; Sekelsky and McIntosh, 1996). MMCR extensively works at frequencies of about 35 GHz (Ka-band) and 94 GHz (W-band) now that the two bands are the atmospheric window with low propagation attenuation owing to less atmospheric absorption. W-band MMCR has smaller and lighter hardware components, which favors their use on airborne and satellite systems, while Ka-band radar is commonly used for ground-based systems, and gains an essential advantage in detecting cirrus above light precipitation because of its less attenuation of ice crystals and snowfall produce (Kropfli et al., 1995). Long-term continuous observation collected from MMCR can provide an insight into the general features of cloud vertical distribution and the microphysical characteristics of cloud formation and development (Uttal et al., 1995; White et al., 1996; Zhao et al., 2017).

Based on measurements from a single-polarization, Doppler cloud radar operating at 35 GHz, Moran et al. (1998) presented a few cloud examples to show its remarkable ability to detect multiple layers of ice and liquid water clouds. Görsdorf et al. (2015) presented data processing in detail for 35 GHz cloud radar, and demonstrated that MMCR datasets are appropriate for investigating cloud climatology, model verification, and satellite validation over a wide range of meteorological conditions. Field experiments in southern China indicated that Ka-band MMCR can provide more detailed structural information about clouds and weak precipitation associated with Typhoon than S-band weather radar (Zhong et al., 2011), and plays a more key role in high cloud observation relative to C-band weather radar in observing low and middle clouds and heavy precipitation (Liu et al., 2017). Combining a 35 GHz cloud radar and a 482 MHz wind radar, Radenz et al. (2018) estimated vertical air motion and particle terminal velocity within clouds.

Using approximately 4000 h data from Ka-band MMCR at Southern Great Plains (SGP, 36.6°N, 97.5°W) in Oklahoma, Dong et al. (2005) analyzed the seasonal variations of cloud height and thickness, which show that more stratus clouds occur in winter (December to February) and spring (March to May) than in summer (June to August) and autumn (September to November), and cloud altitudes and thicknesses are higher and greater in summer than in winter, with averaged thicknesses of 0.85 km and 0.73 km for day and night, respectively. From longer-term cloud observations at the southern great plains, Kollias et al. (2007) confirmed that the majority of middle clouds are shallow with vertical extent <1 km, meanwhile, single-layered cirrus, middle and low clouds are observed a total of 23% of the radar operating time, and multilayer clouds are observed 20.5% of the operating time. By comparing MMCR measurements with geostationary operational environmental satellite observations over the southern great plains, Xi et al. (2010) reported that occurrence frequencies for both daytime and nighttime low cloud tops are significantly higher in satellite data than in MMCR observations, while during the daytime, high clouds are fewer in satellite data than in radar measurements. Base on ground-based MMCR observations over Tibetan Plateau, low and middle clouds were prevalent, and clouds tended to form frequently at night and dissipate gradually in the daytime with an annual mean occurrence frequency of 65.3% (Zhou et al., 2021), in addition, liquid phase clouds below 1.2 km show a single mode distribution (Zhao et al., 2017). Whereas, using MMCR data at Beijing (39.8°N,116.5°E) in China, analysis indicated that middle and high clouds are dominant, and CTH and radar reflectivity are higher in summer and autumn than in spring and winter (Zhang et al., 2019). CTHs derived from MMCR observations at Beijing are significantly higher than those retrieved from geostationary satellite data (Zhou et al., 2019), and the CTH discrepancy between the MMCR measurements and the MODIS data shows a decreasing trend with increasing height (Huo et al., 2020). At Boseong (34.8°N, 127.2°E) on southern coast of Korea, thin and low density clouds were observed more effectively by Ka-band MMCR compared with ceilometer and communication, ocean and meteorological Satellite (Oh et al., 2016), and mean COF was about 35.9% with a maximum frequency of 50% in June, in which high, middle and low non-precipitating clouds and precipitating clouds account for 9.3%, 7.4%, 2.9% and 16.2% of the total occurrence frequency (Ye et al., 2020), respectively.

In this study, we use a Ka-band MMCR observation to investigate the vertical structure and active features of clouds at Wuhan. Wuhan City, located in the east of Jianghan plain with crisscross rivers and scattered lakes, is an inland megacity in central China, with a resident population of over 12 million. As an inland city dominated by the subtropical monsoon humid climate, there are high cloud activity, abundant rainfall and four distinct seasons, thus the cloud activity and evolution over Wuhan have evidently regional characteristics. The instruments and methodology used are described in Section 2 and Section 3. In Section 4, the vertical distribution and seasonal variation of clouds are discussed in detail. A summary is provided in Section 5.

2. Instruments and data

The vertical structures of clouds are studied by using the MMCR observation from 1 January to 31 December 2020. As a case investigation, the satellite measurement is applied to compare the CTH with the MMCR observation. The MMCR is situated at the Atmospheric Remote Sensing Observatory (ARSO) in Wuhan University (30.5°N, 114.4°E, 70 m above sea level).

2.1. Ka-Band MMCR

The cloud radar established by the ARSO of Wuhan University is a Ka-band frequency-modulated continuous wave Doppler radar. The Ka-band MMCR and its position are shown in Fig. 1. The radar system transmits a mean power of 50 W at operating frequency of 35.035 GHz through 0.38° width beam formed by a Cassegrain antenna with 1.5 m diameter. Echoes from backscattering of cloud particles are received by the other same Cassegrain antenna, and then are sent to the signal processing subsystem to obtain the radial distribution of clouds and their motion parameters, such as reflectivity factor (Z), Doppler velocity, Doppler spectrum width and signal-to-noise ratio. The radar system has a maximum detectable distance of 30.72 km (corresponding to 1024 distance gates), a sensitivity of −30 dBZ at the distance of 10 km, and an

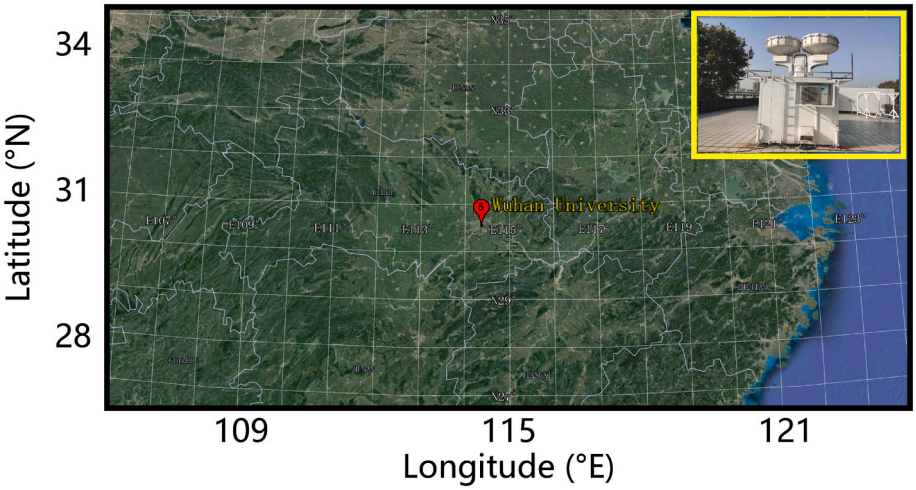

Fig. 1. Ka-band millimeter wave cloud radar in Wuhan University at 30.5°N and 114.4°E.

adjustable maximum unambiguous velocity (up to 20 ms^{-1}) and an adjustable range resolution (5, 10 and 30 m) by modulating and demodulating the continuous wave. The servo-mechanical subsystem can conduct the radar to work at specified directional mode or scanning mode. The cloud radar was deployed in December 2019, and operated at the vertically pointing observation for almost all of 2020. There are no occlusions over the MMCR, and both receive and transmit antennas are surrounded by a metal cylinder with height of 0.45 m, as shown in Fig. 1, thus ground clutter signals can be significantly filtered out for the vertically pointing observation since the Ka-band microwave has a good linear propagation characteristic. The radar observations are recorded in a temporal interval of 0.27 s with a vertical resolution of 30 m, and the 1-min average reflectivity factor is used in the study. Here, the average reflectivity is obtained through exponential and logarithmic transformation from the radar records in units of dBZ since the reflectivity is a quantity in logarithm. In addition, the calibration of the MMCR system is carried out by a 0.2-μs testing signal (corresponding to 30-m distance gate) fed to the front end of the receiver.

2.2. Satellite data

Himawari-8 satellite is a geostationary meteorological satellite over 140°E, launched in October 2014 by Japan Meteorological Agency. The satellite was equipped with advanced Himawari imagers (AHIs), with spatial resolutions from 0.5 to 2.0 km and temporal resolutions from 2.5 to 10 min (Bessho et al., 2016). Cloud mask product was retrieved from the AHIs data (Heidinger and Sraka, 2012), and clouds were identified from the cloud mask product (Yang et al., 2020). The CTH data has a spatial resolution of 5 km and a temporal resolution of 10 min, and research product of CTH used in this paper was supplied by the P-Tree System, Japan Aerospace Exploration Agency at the website of https://www.eorc.jaxa.jp/ptree/index.html.

3. Methodology

3.1. Methods

We use the reflectivity factor of the vertically pointing measurements to investigate the vertical structures of non-precipitation clouds, thus the precipitation and non-precipitation clouds are separated from the cloud observation. In previous studies, $Z = -10$ dBZ near the ground is generally chosen as the threshold to identify precipitation in the MMCR observations (Wang and Sassen, 2001; Zheng et al., 2019). In order to minimize misjudgment from echo signal from a single distance gate, $Z \geq$-10 dBZ in the first five distance gates is selected to be the threshold to identify precipitation. The thresholds of Z=-30 dBZ and Z=-40 dBZ are used to distinguish non-precipitation cloud echo from non-cloud echo near the ground in different studies (Oh et al., 2016; Wang et al., 2018a; Zhang et al., 2019; Ye et al., 2020), respectively. Here, when −40 dBZ$<Z<$-10 dBZ in the first five gates, we determine that there is the non-precipitation cloud near the ground. Of cause, it is hard to distinguish accurately between non-precipitation cloud and non-cloud near the surface, and we discuss the possible contamination in the statistics. Similarly, for reducing the misjudgment in the CTH and CBH of non-precipitation cloud, if $Z>$-40 dBZ in consecutive five distance gates, the cloud is identified, and the height of the first gate in the five distance gates is viewed as the CBH. And then, with height increasing, when $Z \leq$-40 dBZ in consecutive five distance gates, the height of the gate before the five distance gates is the CTH. Nevertheless, two layers of clouds with a vertical interval <300 m are merged into one layer (Wang et al., 2018).

The different types of clouds play the different roles in radiative forcing and energy exchange (Hartmann et al., 1992; Oreopoulos and Rossow, 2011). According to the World Meteorological Organization's International Cloud Atlas, mutually exclusive ten cloud genus were defined, organized into three groups: low (LC), middle (MC), high (HC) clouds corresponding to the typical CBHs above the surface. Hence, non-precipitation clouds are organized into three groups: LC, MC and HC. When the CBH is higher 6 km, the clouds are classified as HC, and if the CBH is between 2 km and 6 km, the clouds are referred to as MC. For the clouds with the CBH <2 km, they are regarded as LC.

3.2. Example of observational comparison

Fig. 2 shows the MMCR reflectivity factor from 6:00 to 20:00 LT (same below) on 17 October 2020, together with the cloud top location observed by Himawari-8 satellite. The AHIs on Himawari-8 satellite can provides the cloud top data over Wuhan in 7:40–16:50 of the daytime. The CTHs from the AHIs are depicted in Fig. 2 with the magenta triangles. It can be seen that the cloud tops in the satellite observation are largely consistent with those in the MMCR measurement. In the durations of about 8:00–9:00 and 13:00–15:00, the CTHs from the satellite data are a little larger than those from the radar data, while in the time intervals of about 10:00–13:00 and 15:00–16:00, the cloud tops in the radar observation are generally higher than those in the satellite data. In particular, at 10:50 and 13:00, although the clouds are not only thick but also dense owing to the large values of reflectivity factor, the CTHs of 9.20 and 9.47 km in the MMCR measurement are much higher relative to those of 7.70 and 8.11 km in the satellite observation, which are consistent with the results in previous studies that the CTHs for optically

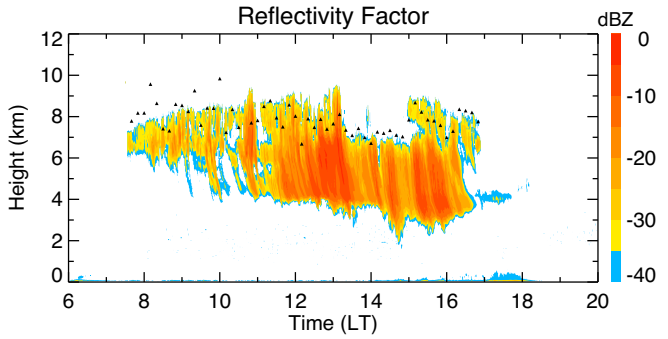

Fig. 2. Reflectivity factor from cloud radar from 6:00 to 20:00 on 17 October 2020. The black triangles represent the cloud top in the satellite observation over Wuhan in the daytime of only 7:20–16:50, respectively.

thick ice clouds retrieved from infrared radiating brightness temperature generally about 1–2 km lower than those from the MMCR observation (Minnis et al., 2008; Wang et al., 2018; Zhang et al., 2019; Huo et al., 2020). Hence, the different CTHs between the satellite and radar data may be due mainly to the coarse spatial resolution and retrieve from infrared channel in the satellite measurements, thus the Ka-band MMCR data is suitable for the investigation of the vertical structures of non-precipitation clouds.

4. Cloud statistics

4.1. Proportions of precipitation and non-precipitation clouds

Based on the above methods, we identify the precipitation and non-precipitation clouds from the radar observations. Fig. 3 presents the monthly percentage of the MMCR operating time and the monthly proportions of precipitation and non-precipitation cloud occurrences to the radar observation in each month. In most months, the missing observation is hours to tens of hours, with a longest period of about 40 h in October, thus on the whole, the missing measurement is not severe in the statistics. In June and July called the plum-rain season, the occurrence probability of precipitation reaches the peak value of 16.3% in July (13.7% in June) as monsoon rain bands linger over Wuhan. As the rain bands move northward and then back, the occurrence frequency of precipitation decreases to 2.6% in August and then rises to 12.2% in September, and accordingly, at Beijing with a higher latitude, the precipitation frequency shows an obvious increase from July to August (Zhang et al., 2019). Another maximal frequency of 14.7% arises in January because precipitation increases as strong cold air frequently moves southwards from frigid Siberia. With temperature rise and moisture increase, the percentage of total precipitation and non-precipitation clouds grows gradually from 53.9% in January to 71.5% in July. Similarly, the non-precipitation cloud increases gradually from 39.2% in January to 55.2% in July, except slightly less probability in June than in May due to the precipitation cloud enhancement in June. The proportion drops to 31.8% in August, and subsequently return to 51.7% in September. Over the year, the average probabilities of precipitation and non-precipitation clouds are about 9.5% and 44.5%, respectively, indicating a humid, cloudy and rainy climate at Wuhan, due to the significant influence of monsoon. At Beijing, the precipitation clouds have a mean frequency of 18.5% with high precipitation rates between August and October (Zhang et al., 2019). On the southern coast of Korea, the frequencies of precipitation and non-precipitation clouds are about 16.2% and 19.7% with their maximum (minimum) values in summer (winter) (Ye et al., 2020), respectively, and similarly, the observations in Xi'an (34.22°N, 108.98°E) show the maximum and minimum cloud cover in summer and winter (Yuan et al., 2022), respectively. Hence, at these stations in east Asia, the cloud occurrence is more frequent in hot summer than in cold winter, though there are some differences in the frequencies and periods of precipitation due to the influences of monsoon and circulation. In contrast, at an SGP site in Oklahoma, the occurrence probability of clouds varies from a minimum of 39.8% in summer to a maximum of 54.6% in winter with a mean value of 46.9% (Xi et al., 2010).

For the precipitation and non-precipitation clouds, we calculate the distribution of their occurrence frequencies in the reflectivity factor and height section in four seasons. The occurrence frequency is defined as the ratio of the number of precipitation and non-precipitation cloud counts detected by the MMCR in a bin composed of the radar range gate of 30 m and the reflectivity factor increasement of 1 dBZ to the total number of precipitation and non-precipitation cloud counts during the period of a season, respectively. Similar to previous studies (Fu et al., 2003; Guo et al., 2018; Zhang et al., 2019), the frequencies of precipitation and non-precipitation clouds are calculated from the expression as follows,

$$f(i,j) = \frac{N_{dBZ}(i,j)}{\sum_{i=1}^{m}\sum_{j=1}^{n} N_{\mathrm{dBZ}}(i,j)} \quad (1)$$

where $N_{dBZ}(i,j)$ is the total number of precipitation or non-precipitation cloud counts in the j^{th} dBZ (interval of 1 dBZ) at the i^{th} level (interval of 30 m) during a season period, and $f(i,j)$ is the normalized occurrence frequency of the j^{th} dBZ at the i^{th} level for the precipitation or non-precipitation clouds. Fig. 4 shows the reflectivity and height section of occurrence frequency of precipitation clouds in four seasons. The red curve denotes the average reflectivity factor at each height. The average

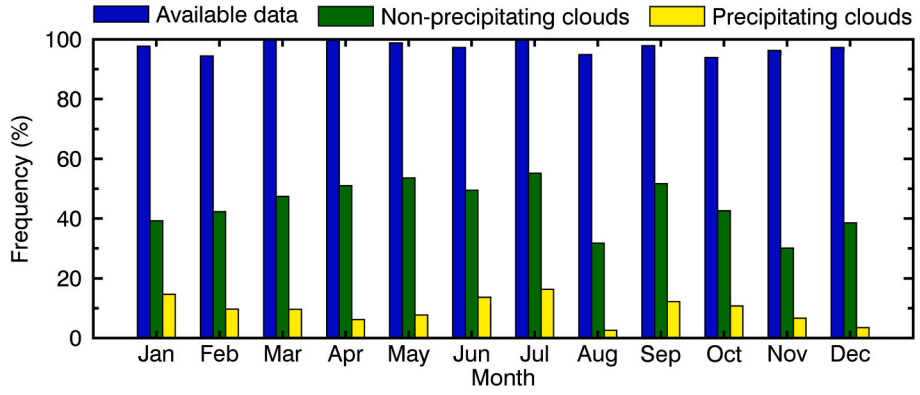

Fig. 3. (blue) Monthly percentage of radar operating time and monthly occurrence frequencies of (yellow) precipition and (green) non-precipitation clouds. The cloud occurrence frequency is calculated relative to the radar operating time. (For interpretation of the references to colour in this figure legend, the reader is referred to the web version of this article.)

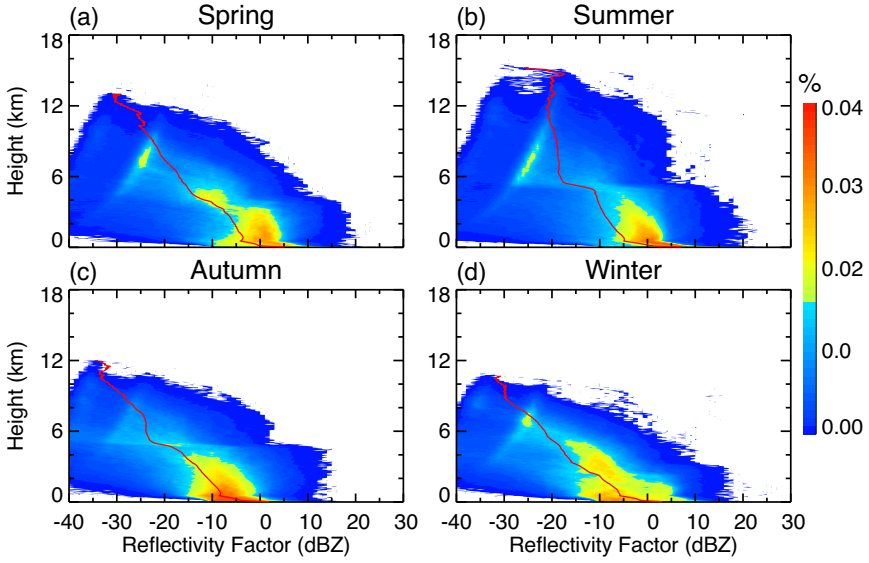

Fig. 4. Reflectivity factor and height section of occurrence frequency of precipitation clouds in (a) spring, (b) summer, (c) autumn and (d) winter. The colour shading represents the occurrence frequency, and the red curve denotes the mean reflectivity factor at each height. (For interpretation of the references to colour in this figure legend, the reader is referred to the web version of this article.)

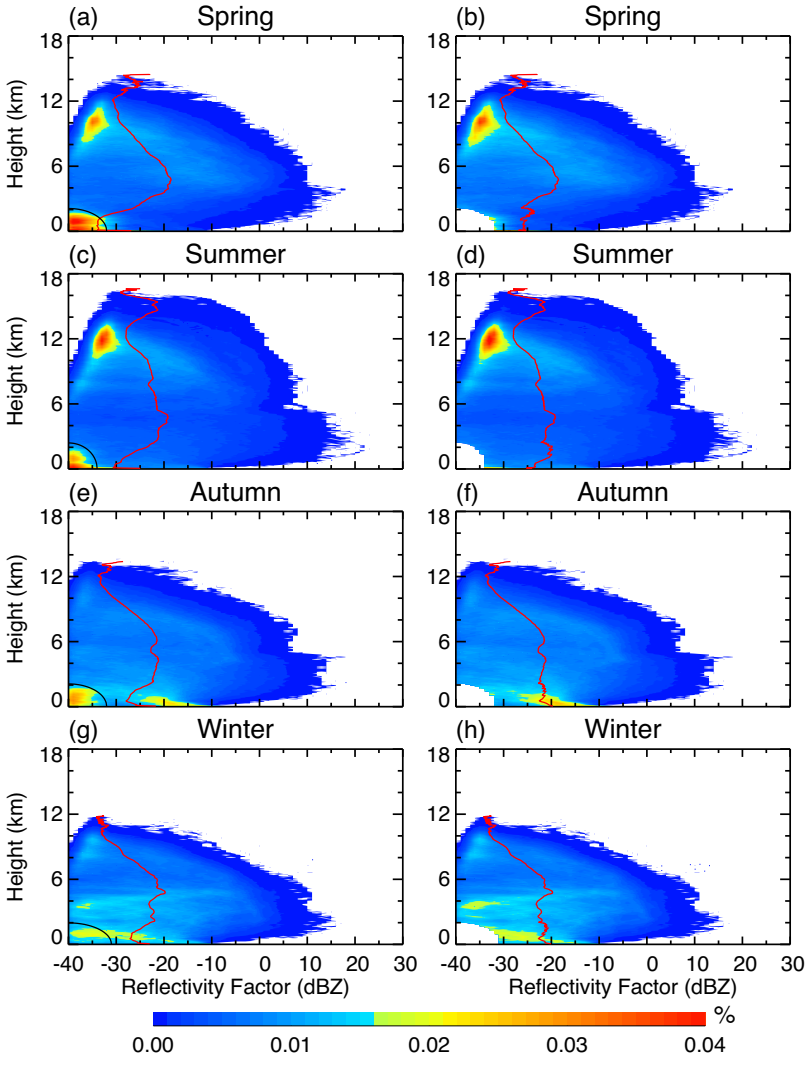

Fig. 5. Reflectivity factor and height section of occurrence frequency of non-precipitation clouds in (a, b) spring, (c, d) summer, (e, f) autumn and (g, h) winter. In the left column, the frequency is derived from the threshold of −40 dBZ, and the quarter ellipse in the bottom-left corner represents the part contaminated by aerosol particles. The frequency in the right column is calculated after removing the contaminated part. The colour shading represents the occurrence frequency, and the red curve denotes the mean reflectivity factor at each height. (For interpretation of the references to colour in this figure legend, the reader is referred to the web version of this article.)

reflectivity increases with height decreasing in all four seasons, indicating the essential feature of hydrometeor size/concentration growth in the precipitation process due to water vapor condensation and raindrop collision and coalescence. It can be seen from Fig. 4 that the average reflectivity near the ground is slightly stronger in summer (7.0 dBZ) and spring (5.2 dBZ) than in winter (3.1 dBZ) and autumn (1.9 dBZ), meanwhile, the peak of occurrence frequency is located at about 0 dBZ in summer and spring, but at about −8 dBZ in winter and autumn, suggesting more intense precipitation in summer and spring. Furthermore, in spring and summer, as the ascending motion intensified by rising temperatures, the precipitation clouds can reach the heights of 13.32 and 15.21 km, which are higher than those of 12.0 and 10.68 km in autumn and winter, respectively. At Wuhan, the mean temperature is about 30 °C in hot summer (Jin et al., 2021), and then bright band height for precipitation is estimated to be around 5 km under a temperature lapse rate of about 6 °C km^{-1}. The bright band in summer can clearly be seen in Fig. 4, and the average reflectivity shows an increasement of 7.1 dBZ between below and above the brightness band. A similar increasement of about 5.6 dBZ occurs in autumn. Whereas, the phenomenon is not very clear in spring and winter, possibly owing to large temperature variation within a season. In addition, there are the maximal values of the occurrence probability above about 5 km with the reflectivity between about −30 and − 20 dBZ, showing the preferential height vs. intensity distribution of precipitation clouds. This distribution pattern might be associated with not only the microphysical processes of condensation, coalescence, vaporization and evaporation, but also the atmospheric conditions of temperature, updraft, and water vapor transport and distribution.

Figure 5 depicts the reflectivity factor and height section of occurrence frequency of non-precipitation clouds in four seasons. The left column in Fig. 5 presents the COF derived from the threshold of −40 dBZ chosen as the basis for determining near-surface clouds. In the MMCR measurement, echoes from near-surface aerosol particles are generally less than −40 dBZ, but there are also some strong echoes between −40 and − 30 dBZ, as show in Fig. 2, which can cause an increase of clouds detected near the ground due to this misdiagnosis. Whereas, the misdiagnosis is very clear at the lower-left corner on the left panels in Fig. 5, thus we take a quarter ellipse to exclude this part in each season. The axis lengths of ellipse vary slightly in different seasons, for instance, the cutoff height and reflectivity are selected to be 2.4 km and − 34 dBZ in summer and 2.0 km and − 31 dBZ in winter because the aerosol distribution is closely related to the boundary layer height affected by temperature. The right column in Fig. 5 presents the occurrence probability after removing the part contaminated by aerosols. In general, the aerosol influence is not very severe in the statistics except on near-surface clouds by comparing the left and right columns in Fig. 5. In the analysis of non-precipitation clouds, including in Fig. 3, the aerosol influence is removed. For non-precipitation clouds, the maximum height is higher in summer and spring relative to in winter and autumn, similar to that for precipitation clouds. The maximum altitudes of 14.49, 16.62, 13.38 and 11.73 km from spring to winter are 1.17, 1.41, 1.38 and 1.05 km higher than those for precipitation clouds, respectively. The attenuation of radar signals by precipitation is one possible reason for the slightly lower maximum height of precipitation clouds in the radar observations (Moran et al., 1998; White et al., 1996). In summer (spring), relative to the precipitation clouds above bright band around 5 km, the non-precipitation clouds have the obvious occurrence peak at the higher altitude of about 12 (10) km but with the weaker reflectivity factors of −35 to −30 dBZ (−37 to −32 dBZ), indicating that relative to non-precipitation clouds, precipitation clouds tend to develop at lower altitudes. In autumn and winter, the COF near the ground increases due likely to lots of radiation fog in the morning (Duan and Barros, 2017) and frequent near-ground inversion layers (Li et al., 2019; Li et al., 2012). Above 5 km, the average reflectivity of non-precipitation clouds shows an enhancement trend with decreasing height, similar to the precipitation clouds. Below 5 km, the average reflectivity maintains small fluctuations (even decreases in spring) until near surface, which is obviously different from the rapidly strengthening reflectivity of precipitation clouds.

4.2. CBH and CTH of non-precipitation clouds

For non-precipitation clouds, we analyze the cloud base and top distributions. Fig. 6 shows the variation of CBH and CTH occurrence frequencies with height in four seasons, and the occurrence frequency is calculated within a height interval of 1 km. In summer, the cloud top can reach the height of 16–17 km with a frequency of 0.13%. The maximum frequency is 19.07% at 12–13 km for the CTH and 14.51% at 7–8 km for the CBH, while the probabilities of the CTH between 9 km and 11 km are dominant at Beijing (Zhang et al., 2019), indicating a stronger convection due to solar radiation heating at Wuhan with a lower latitude in summer. The percentage of CTH above 7 km is as high as 80.88%, and the proportion of CBH above 6 km accounts for 73.76%. In the lower heights, the CTH and CBH have the submaximal frequencies of only 5.87% at 3–4 km and 6.36% at 2–3 km, respectively, thus the HC is predominant in summer due to intense solar radiation and summer monsoon (Li et al., 2016). From summer to winter, the cloud heights reduce gradually. In autumn, the CTH and CBH mainly distribute between 2 and 10 km without prominent peak. By comparison, in winter, the frequency peaks of CTH and CBH are remarkable with the values of 23.92% at 4–5 km and 23.61% at 2–3 km, respectively. Besides, the CBH below 2 km is the most in winter (20.65%). In spring, the frequency distributions of CTH and CBH are roughly similar to those in autumn but with a slightly upward shift owing to the updraft strengthening, which agrees with the observations at Beijing that it is challenging to discriminate between the frequency distribution patterns in spring and autumn (Zhang et al., 2019).

We calculate the monthly mean and median values of CTH, CBH and CLT, and their 25th and 75th percentile positions, which are shown by the box diagram in Fig. 7, together with their maximum and minimum values. The maximum CTH (CBH) gradually rises from 11.1 (10.8) km in January to 16.62 (16.26) km in July, and then fall to 11.49 (10.86) km in December. The mean and median CTH and CBH show a seasonal variation of first increasing and then decreasing, similar to the changes of their maximum values but with the peak height in August instead of July. In the warm months from May to September, the medium values of both CTH and CBH are slightly larger than the mean values, indicating the upward development of clouds because of their modes at higher positions. In contrast, in the other months, the medium values tend to be slightly lower relative to the mean values, especially for CBH. Similar annual cycle of CBH can be seen in the lidar observations over Taihu (31.27°N, 120.21°E) (Liu et al., 2015). At Beijing, the mean CTH is also slightly larger in the warm months than in the cold months but the peak of mean CBH arises in spring, and the contrasts between the CBHs and CTHs in different seasons are attributed to differences in solar radiation (Zhang et al., 2019). As for the CLT, the maximum value of 15.81 km occurs in June. The mean (median) CLT has the largest thickness of 2.18 (1.53) km in May and September (May), and the smallest thickness of 1.36 (0.9) km in November (November), thus the monthly variation of CLT is different from those of CTH and CBT, which are consistent with the results in early studies that the CLT can be impacted by cloud altitudes and formation mechanisms besides temperature and water vapor (Comstock et al., 2002; Pandit et al., 2015; Zhang et al., 2019; Barreto et al., 2022).

4.3. Diurnal variation of non-precipitation clouds

We calculate the diurnal evolution of seasonally average non-precipitation cloud occurrence frequency. Fig. 8 depicts the hourly occurrence frequency of non-precipitation clouds in four seasons and the whole year, and the frequency values are marked at half an hour. There are two prominent features, i.e., a high occurrence frequency (>50%)

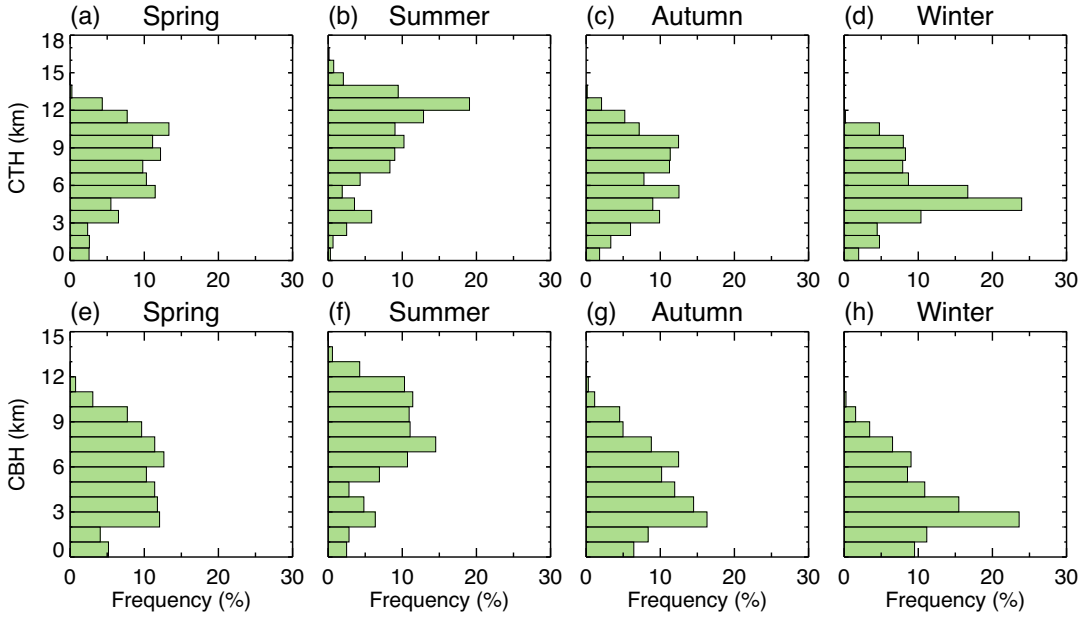

Fig. 6. Vertical distributions of cloud top and base occurrence frequencies in (a, e) spring, (b, f) summer, (c, g) autumn and (d, h) winter. The upper and lower rows represent the cloud top and base heights, respectively.

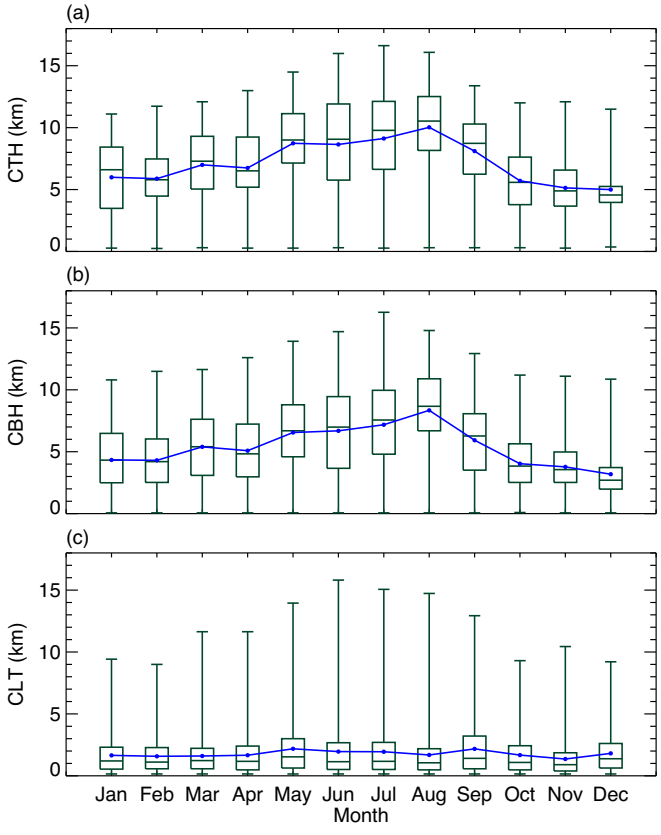

Fig. 7. Monthly mean, median, and 25th and 75th percentile positions of (a) top and (b) base heights and (c) thickness for non-precipitation clouds. The upper and lower sides of the box denote the 25th and 75th percentile positions, and the short line and blue dot inside the box denote the median and mean values, respectively. The short dashes above and below the box represent the heights of the maximum and minimum values, respectively. (For interpretation of the references to colour in this figure legend, the reader is referred to the web version of this article.)

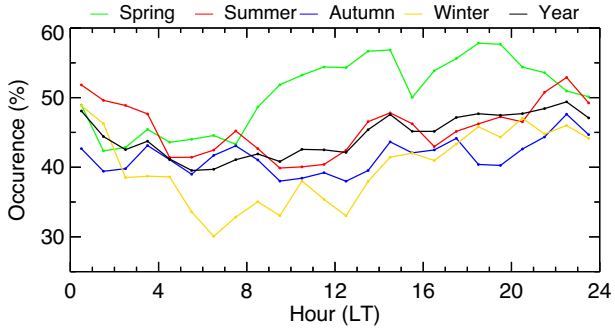

Fig. 8. Diurnal variation of non-precipitation cloud occurrence frequency in (green) spring, (red) summer, (blue) autumn, (orange) winter and (black) whole year. (For interpretation of the references to colour in this figure legend, the reader is referred to the web version of this article.)

from 10:00 to 22:00 in spring, and a low frequency (<39%) from 2:00 to 14:00 in winter. In spring, the COF increases from 43.3% during 7:00–8:00 in the morning to about 56.8% during 13:00–15:00 in the afternoon, whereas subsequently decreases to 50.04% during 15:00–16:00 and then rises again to the maximum value of about 57.8% during 18:00–20:00 in the evening. In winter, there is a rapid reduction from 48.84% during 0:00–1:00 to 30.07% during 6:00–7:00. In autumn, the COF fluctuates slightly throughout 24 h with the maximum proportion of 47.61% during 22:00–23:00 and the minimum fraction of about 38% during 9:00–13:00. In both summer and winter, the occurrence rate shows a descending trend before 6:00 and a slowly ascending trend after 16:00, and maintains a relatively low fraction with fluctuations at other hours of the daytime. A similar diurnal variation can also be seen in the COF over the whole year but with smaller change amplitudes between 39.5% during 5:00–7:00 and 49.4% during 22:00–23:00. On the southern coast of Korea, the diurnal variation of MC and HC exhibits an evident drop of COF around noon, especially in spring (Ye et al., 2020), and the decrease of COF around noon is reported in the CBH observations over Taihu (Liu et al., 2015), whereas, the LC fraction shows an obvious rise around noon over Oklahoma (Dong et al., 2005).

Figure 9 presents the diurnal variation of the seasonally mean and median values of top and base heights and thickness for the non-precipitation clouds at four seasons. It can be seen that throughout 24 h, the mean and median CTH and CBH variations are small. The mean CTH (CBH) is around about 7 (5.5), 9 (7.5), 6.5 (4.8) and 5.5 (4.0) km from spring to winter, thus the mean CLT is by and large between 1.5 and 1.7 km. Hence, both the mean and median CTH and CBH are the highest in hot summer and the lowest in cold winter, and are larger in spring with rising temperature than in autumn with falling temperature. The diurnal variation of the mean CTH (CBH) has the largest values of 0.59 (0.47) km in spring, and is 0.39 (0.24), 0.46 (0.24), and 0.34 (0.39) km in summer, autumn and winter, respectively. The mean CLT has the small diurnal changes of 0.22, 0.21, 0.29 and 0.09 km from spring to winter, respectively. The median CLT is generally 0.5–0.7 km lower than the mean CLT in four seasons, and the median value of CLT is slightly higher in winter and spring relative to in summer and autumn. It is interesting that in summer, the median CTH is higher than the mean CTH, but the opposite is true in winter; in contrast, the median value exceeds the mean value after 9:00 in spring and 10:00 in autumn, indicating the maximum frequency of the CTH moves up with temperature rise. The relation between the mean and median CBHs show a similar characteristic except in autumn. These results show the response of clouds to seasonal and diurnal variations of temperature.

4.4. Three groups of non-precipitation clouds

Finally, we investigate further the occurrence frequency and vertical distribution of three types of non-precipitation clouds. The occurrence frequency is calculated relative to the radar operating time. Fig. 10 shows the occurrence frequencies of high, middle and low clouds in each

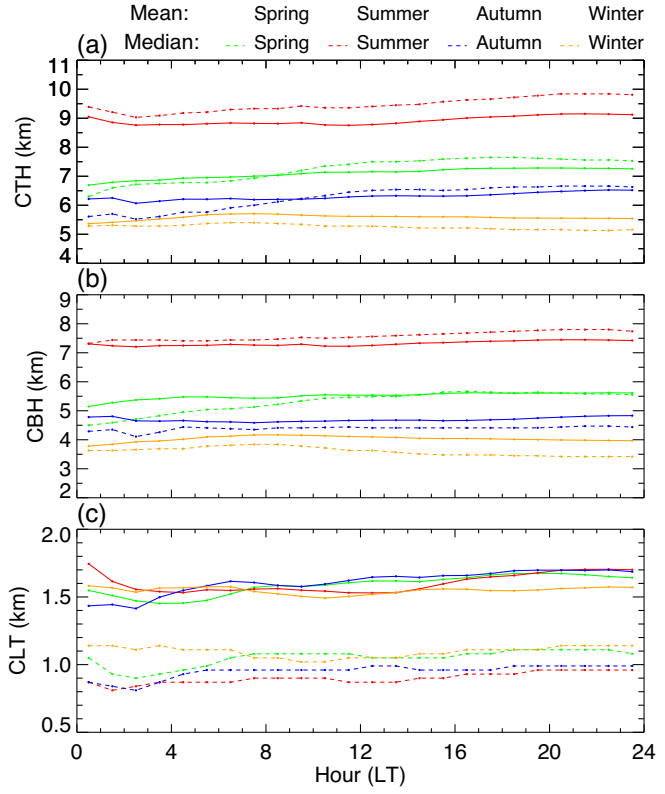

Fig. 9. Diurnal variation of (solid) mean and (dashed) median values of (a) top and (b) base heights and (c) thickness for non-precipitation clouds with local time in (green) spring, (red) summer, (blue) autumn and (orange) winter. (For interpretation of the references to colour in this figure legend, the reader is referred to the web version of this article.)

month and the whole year. The HC is predominant in the warm months from May to September with the proportion exceeding 32%. Its maximum probability of 46.3% appears in July, nevertheless, the HC with respect to the monthly total cloud occurrence has the highest proportion of 77.1% in August. The fraction of HC experiences a remarkedly drop from 32.5% in September to only 8.91% in October, and then is less than those of both HC and LC from October to February. From October to April, the MC is the most abundant clouds, with the peak of 30.8% in April. The LC has the maximum probability of 21.3% in January, close to that of MC (21.2%). For the MC and LC, their lowest occurrence probability occurs in August. Over the whole year, the occurrence frequencies of HC (23.2%) and MC (22.6%) are far more than that of LC (15.1%). Hence, the HCs and MCs are the dominant clouds in the subtropical site since the higher temperature is conducive to the cloud development toward higher height. On the southern coast of Korea, the HC and MC have the smaller frequencies of 9.34% and 7.41%, respectively, but their frequencies are also much larger than that (2.93%) of LC (Ye et al., 2020). The dominant HC and MC are observed at Beijing (Zhang et al., 2019), too. In Oklahoma, the LC has a lower probability but with higher CTH and CBT and greater CLT in summer than in winter (Dong et al., 2005). In addition, small changes in the cloud-radiative forcing fields can play a significant role as a climate feedback mechanism (Ramanathan et al., 1989). HCs have generally the greenhouse effect since solar shortwave radiation passes more easily through their ice crystal particles than longwave radiation from the surface and lower atmosphere, on the contrary, LCs have the cooling effect because more solar radiation is reflected by their water droplets than transmitted. Therefore, the cloud distribution with the dominant HC and MC might have a net heating effect on the climate, which can be estimated quantitatively by cloud-radiative forcing models (Norris et al., 2016; Ceppi and Nowack, 2021).

Figure 11 presents the mean, median, and 25th and 75th percentile positions of top and base heights and thickness for the high, middle and low clouds in the whole year. The mean (median) CTHs of HC, MC and LC are 10.08 (9.99), 5.62 (5.22) and 3.10 (1.98) km, and their mean (median) CBHs are 8.58 (8.28), 3.81 (3.63) and 1.02 (0.99) km, respectively. At Beijing, both the mean CTH (9.45 km) and CBH (7.80) of HC are slightly lower relative to those at Wuhan, whereas the mean CBHs (4.20 and 1.27 km) of MC and LC is slightly higher (Zhang et al., 2019), showing the regional differences. The maximum CTHs of HC, MC and LC can rise to 16.62 km in July, 16.05 km in August and 16.14 km in August, respectively, and the CBH of cirrus clouds can reach 16.26 km in summer, close to the tropopause at about 17 km, implying abundant moisture and strong updraft at Wuhan in summer. The mean CLT of 2.19 km for LC is larger than those of 1.50 km for HC and 1.82 km for MC. The median CLTs of LC, MC and HC are 1.17, 1.17 and 1.05 km, respectively.

5. Summary

In this paper, we firstly investigate the characteristic of cloud vertical structures, such as COF , CBH, CTH and CLT, and their seasonal variation at Wuhan in central China from the vertically pointing observations of the Ka-band frequency-modulated continuous MMCR of Wuhan University in 2020.

Over Wuhan, precipitation is significantly influenced by monsoons. The precipitation has the mean occurrence frequency of 9.5% in 2020. Its peak of 16.3% occurs in July of the plum-rain season when the southeast monsoon brings abundant moisture, and the submaximal frequency of 14.7% arises in January owing to the frequent cold air from the north. The percentage of precipitation and non-precipitation clouds increases gradually from 53.9% in January to a large value of 71.5% in July. The seasonal variation tend of precipitation and non-precipitation clouds is roughly consistent with the observations at higher latitude stations in the east Asia, but their frequency is larger at Wuhan than at these stations, showing the climatic feature of humid, cloudy and rainy

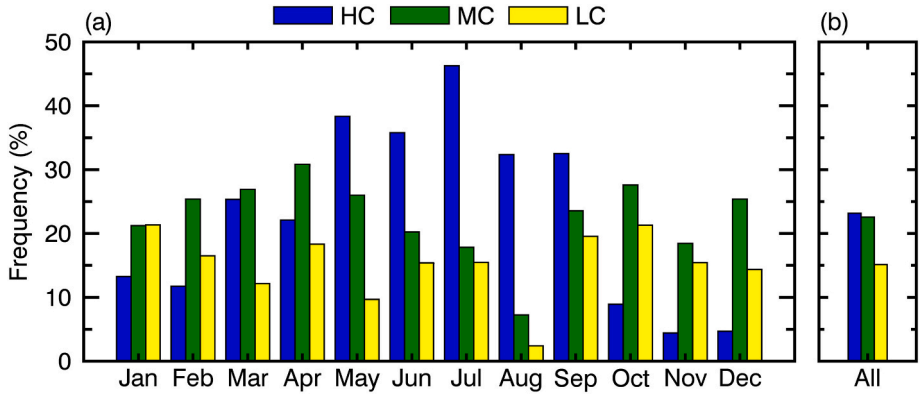

Fig. 10. (a) Monthly and (b) whole year occurrence frequencies of (bule) high, (green) middle and (yellow) low clouds. (For interpretation of the references to colour in this figure legend, the reader is referred to the web version of this article.)

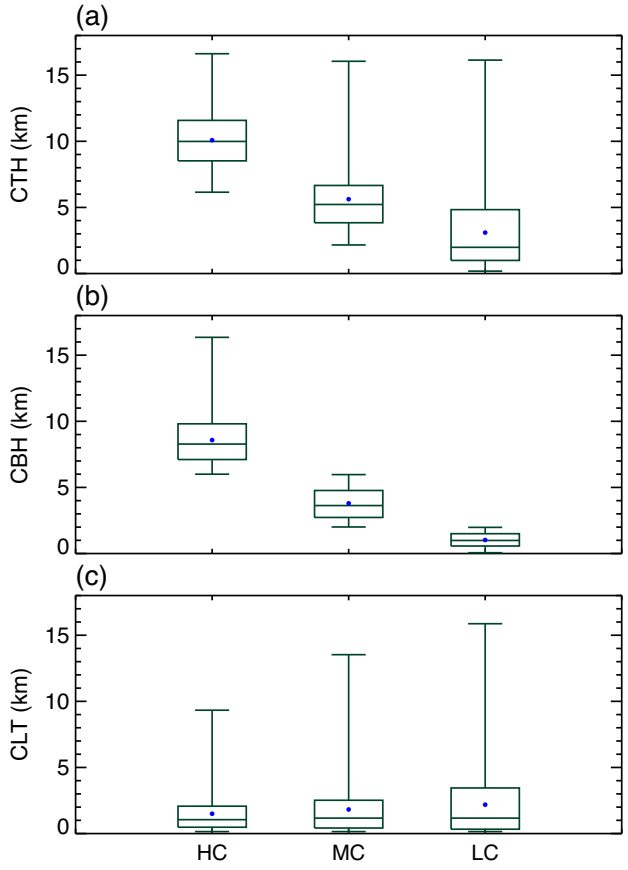

Fig. 11. Mean, median, and 25th and 75th percentile positions of (a) top and (b) base heights and (c) thickness for high, middle and low clouds. The upper and lower sides of the box denote the 25th and 75th percentile positions, and the short line and blue dot inside the box denote the median and mean values, respectively. The short dashes above and below the box represent the heights of the maximum and minimum values, respectively. (For interpretation of the references to colour in this figure legend, the reader is referred to the web version of this article.)

at Wuhan. In contrast, at an SGP site in America, the probability of clouds has a minimum in summer and a maximum in winter.

The non-precipitation clouds have the occurrence frequency of 44.5% in the year. The COF grows gradually from 39.2% in January to 55.2% in July, whereas, rapidly falls to 31.8% in August and then subsequently returns to 51.7% in September as the monsoons move northward and back. It is interesting that there are two prominent peaks of COF with the reflectivities of −35 to −30 dBZ around 12 km in summer and − 37– −32 dBZ around 10 km in spring. The CTH and CBH have the maximum frequencies of 19.07% at 12–13 km and 14.51% at 7–8 km in summer, and 23.92% at 4–5 km and 23.61% at 2–3 km in winter, respectively. The heights of peak frequency for the CTH are slightly higher relative to those at Beijing with a higher latitude. The monthly mean and median CTH and CBH is the lowest in December, and the highest in August though their maximum values arise in July. The CLT can reach 15.81 km in June, and the monthly mean CLT has the largest thickness of 2.18 km in May and September, and the smallest thickness of 1.36 km in November. Similar annual cycle of CTH and CBH is reported at the other stations in the east Asia.

As for the diurnal evolution, through 24 h, the seasonally mean COF is generally between 40% and 50% in four seasons and over the year, except a high probability (>50%) from 10:00 to 22:00 in spring, and a low probability (<39%) from 2:00 to 14:00 in winter. Around noon, the COF shows a significant decline on the southern coast of Korea but an obvious rise over Oklahoma. The seasonally mean CTH (CBH) is about 7 (5.5), 9 (7.5), 6.5 (4.8) and 5.5 (4.0) km from spring to winter, thus the mean CLT is by and large between 1.5 and 1.7 km. Meanwhile, the median CLT is generally 0.5–0.7 km lower than the mean CLT in four seasons. In summer, the median CTH is higher than the mean CTH, but the opposite is true in winter. The median CTH exceeds the mean CTH after 9:00 in spring and 10:00 in autumn. These results show the response of clouds to seasonal and diurnal variations of temperature.

In three types of non-precipitation clouds, the HC is predominant in the warm months from May to September with the proportion exceeding 32%, and in the other months, the MC is the most abundant clouds with the frequency peak of 30.8% in April. The LC has the maximum probability of 21.3% in January, close to that of MC (21.2%). Over the whole year, the occurrence frequencies of HC, MC and LC account for 23.2%, 22.6% and 15.1%, respectively. The dominant HC and MC are also observed at the higher latitude sites in the east Asia, but relative to the observations at Wuhan, their occurrence probabilities are obviously smaller, and the mean CTH and CBT of HC are slightly lower, showing the regional differences in the cloud activities. Clouds is one of the largest sources of uncertainty in current climate models. Low, middle and high clouds have different effects on short-wave and long-wave radiation, and even there are also differences in their radiative effects between day and night. Hence, the quantitative investigation of low, middle and high clouds and their diurnal variation is helpful in improving the cloud parameterization in climate models.

Declaration of Competing Interest

The authors declare that they have no known competing financial interests or personal relationships that could have appeared to influence

the work reported in this paper.

Data availability

Data will be made available on request.

Acknowledgments

The authors are grateful to the editor and anonymous reviewers for their constructive suggestions and comments on this paper. This work was jointly supported by the National Natural Science Foundation of China (through grants 42174189 and 41974176).

References

Alexander, S.P., Protat, A., 2018. Cloud properties observed from the surface and by satellite at the northern edge of the Southern Ocean. J. Geophys. Res.-Atmos. 123, 443–456. https://doi.org/10.1002/2017JD026552.

Barreto, Á., Cuevas, E., García, R.D., Carrillo, J., Prospero, J.M., Ilić, L., Basart, S., Berjón, A.J., Marrero, C.L., Hernández, Y., Bustos, J.J., Ničković, S., Yela, M., 2022. Long-term characterisation of the vertical structure of the Saharan Air Layer over the Canary Islands using lidar and radiosonde profiles: Implications for radiative and cloud processes over the subtropical Atlantic Ocean. Atmos. Chem. Phys. 22, 739–763. https://doi.org/10.5194/acp-22-739-2022.

Bessho, K., Date, K., Hayashi, M., Ikeda, A., Imai, T., Inoue, H., Kumagai, Y., Miyakawa, T., Murata, H., Ohno, T., Okuyama, A., Oyama, R., Sasaki, Y., Shimazu, Y., Shimoji, K., Sumida, Y., Suzuki, M., Taniguchi, H., Tsuchiyama, H., Uesawa, D., Yokota, H., Yoshida, R., 2016. An introduction to Himawari-8/9 — Japan's new-generation geostationary meteorological satellites. J. Meteor. Soc. Japan. 94, 151–183. https://doi.org/10.2151/jmsj.2016-009.

Cairo, F., De Muro, M., Snels, M., Di Liberto, L., Bucci, S., Legras, B., Kottayil, A., Scoccione, A., Ghisu, S., 2021. Lidar observations of cirrus clouds in Palau (7°33′N, 134°48′E). Atmos. Chem. Phys. 21, 7947–7961. https://doi.org/10.5194/acp-21-7947-2021.

Ceppi, P., Nowack, P., 2021. Observational evidence that cloud feedback amplifies global warming. Proc. Natl. Acad. Sci. 118, e2026290118 https://doi.org/10.1073/pnas.2026290118.

Chang, F.-L., Li, Z., 2005. A near-global climatology of single-layer and overlapped clouds and their optical properties retrieved from Terra/MODIS data using a new algorithm. J. Clim. 18, 4752–4771. https://doi.org/10.1175/JCLI3553.1.

Clothiaux, E.E., Moran, K.P., Martner, B.E., Ackerman, T.P., Mace, G.G., Uttal, T., Mather, J.H., Widener, K.B., Miller, M.A., Rodriguez, D.J., 1999. The atmospheric radiation measurement program cloud radars: operational modes. J. Atmos. Ocean. Technol. 16, 819–827. https://doi.org/10.1175/1520-0426(1999)016<0819:TARMPC>2.0.CO;2.

Clothiaux, E.E., Ackerman, T.P., Mace, G.G., Moran, K.P., Marchand, R.T., Miller, M.A., Martner, B.E., 2000. Objective determination of cloud heights and radar reflectivities using a combination of active remote sensors at the ARM CART sites. J. Appl. Meteorol. Climatol. 39, 645–665. https://doi.org/10.1175/1520-0450(2000)039<0645:ODOCHA>2.0.CO;2.

Comstock, J.M., Ackerman, T.P., Mace, G.G., 2002. Ground-based lidar and radar remote sensing of tropical cirrus clouds at Nauru island: Cloud statistics and radiative impacts. J. Geophys. Res.-Atmos. 107 https://doi.org/10.1029/2002JD002203 (AAC 16-1-AAC 16-14.

Dong, X., Minnis, P., Xi, B., 2005. A climatology of midlatitude continental clouds from the ARM SGP central facility: part I: low-level cloud macrophysical, microphysical, and radiative properties. J. Clim. 18, 1391–1410. https://doi.org/10.1175/JCLI3342.1.

Duan, Y., Barros, A.P., 2017. Understanding how low-level clouds and fog modify the diurnal cycle of orographic precipitation using in situ and satellite observations. Remote Sens. 9, 920. https://doi.org/10.3390/rs9090920.

Ellingson, R.G., 1982. On the effects of cumulus dimensions on longwave irradiance and heating rate calculations. J. Atmos. Sci. 39, 886–896. https://doi.org/10.1175/1520-0469(1982)039<0886:OTEOCD>2.0.CO;2.

Fu, Y., Lin, Y., Liu, G., Wang, Q., 2003. Seasonal characteristics of precipitation in 1998 over East Asia as derived from TRMM PR. Adv. Atmos. Sci. 20, 511–529. https://doi.org/10.1007/BF02915495.

Görsdorf, U., Lehmann, V., Bauer-Pfundstein, M., Peters, G., Vavriv, D., Vinogradov, V., Volkov, V., 2015. A 35-GHz polarimetric doppler radar for long-term observations of cloud parameters—Description of system and data processing. J. Atmos. Ocean. Technol. 32, 675–690. https://doi.org/10.1175/JTECH-D-14-00066.1.

Guo, J., Liu, H., Li, Z., Rosenfeld, D., Jiang, M., Xu, W., Jiang, J.H., He, J., Chen, D., Min, M., Zhai, P., 2018. Aerosol-induced changes in the vertical structure of precipitation: a perspective of TRMM precipitation radar. Atmos. Chem. Phys. 18, 13329–13343. https://doi.org/10.5194/acp-18-13329-2018.

Guo, J., Liu, B., Gong, W., Shi, L., Zhang, Y., Ma, Y., Zhang, J., Chen, T., Bai, K., Stoffelen, A., de Leeuw, G., Xu, X., 2021. Technical note: first comparison of wind observations from ESA's satellite mission Aeolus and ground-based radar wind profiler network of China. Atmos. Chem. Phys. 21, 2945–2958. https://doi.org/10.5194/acp-21-2945-2021.

Han, D., Ellingson, R.G., 2000. An experimental technique for testing the validity of cumulus cloud parameterizations for longwave radiation calculations. J. Appl. Meteorol. Climatol. 39, 1147–1159. https://doi.org/10.1175/1520-0450(2000)039<1147:AETFTT>2.0.CO;2.

Hartmann, D.L., Ockert-Bell, M.E., Michelsen, M.L., 1992. The effect of cloud type on earth's energy balance: global analysis. J. Clim. 5, 1281–1304. https://doi.org/10.1175/1520-0442(1992)005<1281:TEOCTO>2.0.CO;2.

Hawkinson, J.A., Feltz, W., Ackerman, S.A., 2005. A comparison of GOES sounder- and cloud lidar- and radar-retrieved cloud-top heights. J. Appl. Meteorol. Climatol. 44, 1234–1242. https://doi.org/10.1175/JAM2269.1.

Heidinger, A., Sraka, W.C., 2012. Algorithm Theoretical Basis Document ABI Cloud Mask. Available at the website of. https://www.star.nesdis.noaa.gov/goesr/documents/ATBDs/Baseline/ATBD_GOES-R_Cloud_Mask_v3.0_July%202012.pdf.

Huang, Y., 2013. On the longwave climate feedbacks. J. Clim. 26, 7603–7610. https://doi.org/10.1175/JCLI-D-13-00025.1.

Huo, J., Li, J., Duan, M., Lv, D., Han, C., Bi, Y., 2020. Measurement of cloud top height: comparison of MODIS and ground-based millimeter radar. Remote Sens. 12, 1616. https://doi.org/10.3390/rs12101616.

Jin, S., Ma, Y., Gong, W., Liu, B., Lei, L., Fan, R., 2021. Characteristics of vertical atmosphere based on five-year microwave remote sensing data over Wuhan region. Atmos. Res. 260, 105710 https://doi.org/10.1016/j.atmosres.2021.105710.

Kollias, P., Tselioudis, G., Albrecht, B.A., 2007. Cloud climatology at the Southern Great Plains and the layer structure, drizzle, and atmospheric modes of continental stratus. J. Geophys. Res.-Atmos. 112, D9116. https://doi.org/10.1029/2006JD007307.

Krofli, R.A., Kelly, R.D., 1996. Meteorological research applications of MM-wave radar. Meteorl. Atmos. Phys. 59, 105–121. https://doi.org/10.1007/BF01032003.

Kropfli, R.A., Matrosov, S.Y., Uttal, T., Ok, B.W., Frisch, A.S., Clark, K.A., Bartram, B.W., Reinking, R.F., Snider, J.B., Martner, B.E., 1995. Cloud physics studies with 8 mm wavelength radar. Atmos. Res. 35, 299–313. https://doi.org/10.1016/0169-8095(94)00025-9.

Lazarus, S.M., Krueger, S.K., Mace, G.G., 2000. A cloud climatology of the southern great plains ARM CART. J. Clim. 13, 1762–1775. https://doi.org/10.1175/1520-0442(2000)013<1762:ACCOTS>2.0.CO;2.

Li, J., Chen, H., Li, Z., Wang, P., Fan, X., He, W., Zhang, J., 2019. Analysis of low-level temperature inversions and their effects on aerosols in the lower atmosphere. Adv. Atmos. Sci. 36, 1235–1250. https://doi.org/10.1007/s00376-019-9018-9.

Li, Y., Yan, J., Sui, X., 2012. Tropospheric temperature inversion over Central China. Atmos. Res. 116, 105–115. https://doi.org/10.1016/j.atmosres.2012.03.009.

Li, Z., Lau, W.K.-M., Ramanathan, V., Wu, G., Ding, Y., Manoj, M.G., Liu, J., Qian, Y., Li, J., Zhou, T., Fan, J., Rosenfeld, D., Ming, Y., Wang, Y., Huang, J., Wang, B., Xu, X., Lee, S.-S., Cribb, M., Zhang, F., Yang, X., Zhao, C., Takemura, T., Wang, K., Xia, X., Yin, Y., Zhang, H., Guo, J., Zhai, P.M., Sugimoto, N., Babu, S.S., Brasseur, G. P., 2016. Aerosol and monsoon climate interactions over Asia. Rev. Geophys. 54, 866–929. https://doi.org/10.1002/2015RG000500.

Liu, J., Li, Z., Zheng, Y., Cribb, M., 2015. Cloud-base distribution and cirrus properties based on micropulse lidar measurements at a site in southeastern China. Adv. Atmos. Sci. 32, 991–1004. https://doi.org/10.1007/s00376-014-4176-2.

Liu, L., Ruan, Z., Zheng, J., Gao, W., 2017. Comparing and merging observation data from Ka-band cloud radar, C-band frequency-modulated continuous wave radar and ceilometer systems. Remote Sens. 9, 1282. https://doi.org/10.3390/rs9121282.

Martucci, G., Milroy, C., O'Dowd, C.D., 2010. Detection of cloud-base height using Jenoptik CHM15K and Vaisala CL31 ceilometers. J. Atmos. Ocean. Technol. 27, 305–318. https://doi.org/10.1175/2009JTECHA1326.1.

Minnis, P., Yost, C.R., Sun-Mack, S., Chen, Y., 2008. Estimating the top altitude of optically thick ice clouds from thermal infrared satellite observations using CALIPSO data. Geophys. Res. Lett. 35, L12801. https://doi.org/10.1029/2008GL033947.

Moran, K.P., Martner, B.E., Post, M.J., Kropfli, R.A., Welsh, D.C., Widener, K.B., 1998. An unattended cloud-profiling radar for use in climate research. B. Am. Meteorol. Soc. 79, 443–456. https://doi.org/10.1175/1520-0477(1998)079<0443:AUCPRF>2.0.CO;2.

Nazaryan, H., McCormick, M.P., Menzel, W.P., 2008. Global characterization of cirrus clouds using CALIPSO data. J. Geophys. Res.-Atmos. 113, D16211. https://doi.org/10.1029/2007JD009481.

Newell, R.E., Kidson, J.W., Vincent, D.G., Boer, G.J., 1972. The General Circulation of the Tropical Atmosphere and Interactions with Extratropical Latitudes, Volume I and II. Massachusetts Institute of Technology Press, Cambridge, MA.

Norris, J.R., Allen, R.J., Evan, A.T., Zelinka, M.D., O'Dell, C.W., Klein, S.A., 2016. Evidence for climate change in the satellite cloud record. Nature. 536, 72–75. https://doi.org/10.1038/nature18273.

Oh, S.-B., Kim, Y.-H., Kim, K.-H., Cho, C.-H., Lim, E., 2016. Verification and correction of cloud base and top height retrievals from Ka-band cloud radar in Boseong, Korea. Adv. Atmos. Sci. 33, 73–84. https://doi.org/10.1007/s00376-015-5058-y.

Oreopoulos, L., Rossow, W.B., 2011. The cloud radiative effects of International Satellite Cloud Climatology Project weather states. J. Geophys. Res.-Atmos. 116, D12202. https://doi.org/10.1029/2010JD015472.

Pandit, A.K., Gadhavi, H.S., Venkat Ratnam, M., Raghunath, K., Rao, S.V.B., Jayaraman, A., 2015. Long-term trend analysis and climatology of tropical cirrus clouds using 16 years of lidar data set over Southern India. Atmos. Chem. Phys. 15, 13833–13848. https://doi.org/10.5194/acp-15-13833-2015.

Poore, K.D., Wang, J., Rossow, W.B., 1995. Cloud layer thicknesses from a combination of surface and upper-air observations. J. Clim. 8, 550–568. https://doi.org/10.1175/1520-0442(1995)008<0550:CLTFAC>2.0.CO;2.

Quante, M., 2004. The role of clouds in the climate system. J. Phys. IV France 121, 61–86. https://doi.org/10.1051/jp4:2004121003.

Radenz, M., Bühl, J., Lehmann, V., Görsdorf, U., Leinweber, R., 2018. Combining cloud radar and radar wind profiler for a value added estimate of vertical air motion and particle terminal velocity within clouds. Atmos. Meas. Tech. 11, 5925–5940. https://doi.org/10.5194/amt-11-5925-2018.

Ramanathan, V., Cess, R.D., Harrison, E.F., Minnis, P., Barkstrom, B.R., Ahmad, E., Hartmann, D., 1989. Cloud-radiative forcing and climate: results from the earth radiation budget experiment. Science. 243, 57–63. https://doi.org/10.1126/science.243.4887.57.

Sassen, K., Wang, Z., 2008. Classifying clouds around the globe with the CloudSat radar: 1-year of results. Geophys. Res. Lett. 35, L04805. https://doi.org/10.1029/2007GL032591.

Sekelsky, S.M., McIntosh, R.E., 1996. Cloud observations with a polarimetric 33 GHz and 95 GHz radar. Meteorl. Atmos. Phys. 59, 123–140. https://doi.org/10.1007/BF01032004.

Stephens, G.L., 2005. Cloud feedbacks in the climate system: a critical review. J. Clim. 18, 237–273. https://doi.org/10.1175/JCLI-3243.1.

Stephens, G.L., Vane, D.G., Tanelli, S., Im, E., Durden, S., Rokey, M., Reinke, D., Partain, P., Mace, G.G., Austin, R., L'Ecuyer, T., Haynes, J., Lebsock, M., Suzuki, K., Waliser, D., Wu, D., Kay, J., Gettelman, A., Wang, Z., Marchand, R., 2008. CloudSat mission: Performance and early science after the first year of operation. J. Geophys. Res.-Atmos. 113, D00A18. https://doi.org/10.1029/2008JD009982.

Uttal, T., Clothiaux, E.E., Ackerman, T.P., Intrieri, J.M., Eberhard, W.L., 1995. Cloud boundary statistics during FIRE II. J. Atmos. Sci. 52, 4276–4284. https://doi.org/10.1175/1520-0469(1995)052<4276:CBSDFI>2.0.CO;2.

Wang, J., Rossow, W.B., 1998. Effects of cloud vertical structure on atmospheric circulation in the GISS GCM. J. Clim. 11, 3010–3029. https://www.jstor.org/stable/26244244.

Wang, Y., Zhao, C., Dong, Z., Li, Z., Hu, S., Chen, T., Tao, F., Wang, J., 2018. Improved retrieval of cloud base heights from ceilometer using a non-standard instrument method. Atmos. Res. 202, 148–155. https://doi.org/10.1016/j.atmosres.2017.11.021.

Wang, Z., Sassen, K., 2001. Cloud type and macrophysical property retrieval using multiple remote sensors. J. Appl. Meteorol. Climatol. 40, 1665–1682. https://doi.org/10.1175/1520-0450(2001)040<1665:CTAMPR>2.0.CO;2.

Wang, Z., Wang, Z.H., Cao, X., Mao, J., Tao, F., Hu, S., 2018a. Cloud-base height derived from a ground-based infrared sensor and a comparison with a collocated cloud radar. J. Atmos. Ocean. Technol. 35, 689–704. https://doi.org/10.1175/JTECH-D-17-0107.1.

White, A.B., Fairall, C.W., Frisch, A.S., Orr, B.W., Snider, J.B., 1996. Recent radar measurements of turbulence and microphysical parameters in marine boundary layer clouds. Atmos. Res. 40, 177–221. https://doi.org/10.1016/0169-8095(95)00036-4.

Winker, D.M., Vaughan, M.A., 1993. Vertical distribution of clouds over Hampton, Virginia observed by lidar under the ECLIPS and FIRE ETO programs. Atmos. Res. 34, 117–133. https://doi.org/10.1016/0169-8095(94)90084-1.

Xi, B., Dong, X., Minnis, P., Khaiyer, M., 2010. A 10 year climatology of cloud fraction and vertical distribution derived from both surface and GOES observations over the DOE ARM SPG site. J. Geophys. Res.-Atmos. 115, D12124. https://doi.org/10.1029/2009JD012800.

Yan, Y., Liu, Y., Lu, J., 2016. Cloud vertical structure, precipitation, and cloud radiative effects over Tibetan Plateau and its neighboring regions. J. Geophys. Res.-Atmos. 121, 5864–5877. https://doi.org/10.1002/2015JD024591.

Yang, Y., Zhao, C., Fan, H., 2020. Spatiotemporal distributions of cloud properties over China based on Himawari-8 advanced Himawari imager data. Atmos. Res. 240, 104927 https://doi.org/10.1016/j.atmosres.2020.104927.

Ye, B.-Y., Juan, E., Shin, S., Lee, G., 2020. Statistical characteristics of cloud occurrence and vertical structure observed by a ground-based Ka-band cloud radar in South Korea. Remote Sens. 12, 2242. https://doi.org/10.3390/rs12142242.

Young, A.H., Bates, J.J., Curry, J.A., 2013. Application of cloud vertical structure from CloudSat to investigate MODIS-derived cloud properties of cirriform, anvil, and deep convective clouds. J. Geophys. Res.-Atmos. 118, 4689–4699. https://doi.org/10.1002/jgrd.50306.

Yuan, Y., Di, H., Liu, Y., Yang, T., Li, Q., Yan, Q., Xin, W., Li, S., Hua, D., 2022. Detection and analysis of cloud boundary in Xi'an, China, employing 35 GHz cloud radar aided by 1064 nm lidar. Atmos. Meas. Tech. 15, 4989–5006. https://doi.org/10.5194/amt-15-4989-2022.

Zhang, J., Chen, H., Li, Z., Fan, X., Peng, L., Yu, Y., Cribb, M., 2010. Analysis of cloud layer structure in Shouxian, China using RS92 radiosonde aided by 95 GHz cloud radar. J. Geophys. Res.-Atmos. 115, D00K30. https://doi.org/10.1029/2010JD014030.

Zhang, Y., Zhou, Q., Lv, S., Jia, S., Tao, F., Chen, D., Guo, J., 2019. Elucidating cloud vertical structures based on three-year Ka-band cloud radar observations from Beijing, China. Atmos. Res. 222, 88–99. https://doi.org/10.1016/j.atmosres.2019.02.007.

Zhao, C., Liu, L., Wang, Q., Qiu, Y., Wang, Y., Wu, X., 2017. MMCR-based characteristic properties of non-precipitating cloud liquid droplets at Naqu site over Tibetan Plateau in July 2014. Atmos. Res. 190, 68–76. https://doi.org/10.1016/j.atmosres.2017.02.002.

Zheng, J., Liu, L., Chen, H., Gou, Y., Che, Y., Xu, H., Li, Q., 2019. Characteristics of warm clouds and precipitation in South China during the pre-flood season using datasets from a cloud radar, a ceilometer, and a disdrometer. Remote Sens. 11, 3045. https://doi.org/10.3390/rs11243045.

Zhong, L., Liu, L., Feng, S., Ge, R., Zhang, Z., 2011. A 35-GHz polarimetric doppler radar and its application for observing clouds associated with Typhoon Nuri. Adv. Atmos. Sci. 28, 945–956. https://doi.org/10.1007/s00376-010-0073-5.

Zhou, Q., Zhang, Y., Li, B., Li, L., Feng, J., Jia, S., Lv, S., Tao, F., Guo, J., 2019. Cloud-base and cloud-top heights determined from a ground-based cloud radar in Beijing, China. Atmos. Environ. 201, 381–390. https://doi.org/10.1016/j.atmosenv.2019.01.012.

Zhou, R., Wang, G., Zhaxi, S., 2021. Cloud vertical structure measurements from a ground-based cloud radar over the southeastern Tibetan Plateau. Atmos. Res. 258, 105629 https://doi.org/10.1016/j.atmosres.2021.105629.